

The local slip length and flow fields over nanostructured superhydrophobic surfaces

Luyao Bao^a, Nikolai V. Priezjev^b, Haibao Hu^{a,*}

^aSchool of Marine Science and Technology, Northwestern Polytechnical University, Xi'an, Shaanxi 710072, PR China

^bDepartment of Mechanical and Materials Engineering, Wright State University, Dayton, OH 45435, USA

ARTICLE INFO

Article history:

Received 15 May 2019

Revised 19 February 2020

Accepted 29 February 2020

Available online 2 March 2020

Keywords:

Local slip length

Gas-liquid interface

Superhydrophobic surface

Molecular dynamics simulations

ABSTRACT

The local slip behavior and flow fields near the gas-liquid interface (GLI) of a Newtonian liquid flowing past a superhydrophobic surface with periodic rectangular grooves are investigated using molecular dynamics (MD) simulations. The saturated vapor of the liquid fills the groove to form the GLI. A flat GLI is introduced by carefully adjusting the channel height to make the liquid bulk pressure equal to the coexistence pressure. The setup with the flat GLI allows for an accurate determination of the local slip velocity, shear rate and slip length. We find that the local slip velocity and shear rate at the GLI are well described by the elliptical and exponential functions, respectively. By directly computing the local slip length from the local flow fields, we propose a novel distribution function for the slip length along the GLI for both transverse and longitudinal flows. Moreover, we demonstrate that the relationship between the local and the effective slip lengths in the transverse and longitudinal cases deviates from the continuum assumptions as the groove width is reduced to the nanoscale dimensions. The functional form for the local slip length can be potentially used as a boundary condition in the continuum analysis without considering the explicitly gas flow in the grooves of superhydrophobic surfaces.

© 2020 Elsevier Ltd. All rights reserved.

1. Introduction

Recent progress in design of superhydrophobic surfaces (SHS) that are characterized by low surface energy and micro- and nanoscale roughness is important for various applications, including self-cleaning, enhanced mixing, amplified diffusion-osmotic flow and especially drag reduction (Rothstein, 2010). A number of studies have demonstrated that SHS lead to a significant effective slip length in laminar flow (Ou and Rothstein, 2005; Gogte et al., 2005; Choi and Kim, 2006; Byun et al., 2008; Feuillebois et al., 2009; Crowdy, 2011; Busse et al., 2013). In appropriate conditions, e.g., the channel height is comparable to the groove depth in laminar inner channel flows, the effective slip length can produce significant drag reduction (Song et al., 2014). For turbulent flows, the drag reduction was also widely observed because of from the slip length on superhydrophobic surface (Martell et al., 2010; Nouri et al., 2013; Park et al., 2014; Srinivasan et al., 2015; Zhang et al., 2015; Im and Lee, 2017; Costantini et al., 2018; Gose et al., 2018; Rastegari and Akhavan, 2019). Moreover, the superhydrophobic effect is present for surfaces with textures on mul-

multiple length scales, thus extending the range of applications for drag reduction from micro/nano fluidic devices to marine vessels. The key idea behind drag reduction of SHS is the presence of the gas phase trapped at the micro/nano scale structures resulting in enhanced slippage at the gas-liquid interface (GLI). Therefore, in order to predict accurately the fine features of liquid flows over GLI, the explicit knowledge of the local slip condition at SHS is required.

The problem of liquid slip at a solid surface dates back to the times of Navier in 1823. He proposed that the slip velocity, v_s , is proportional to the shear rate at the solid-liquid interface, i.e., $v_s = L_s \dot{\gamma}$, where $\dot{\gamma}$ is the shear rate and L_s is the slip length. In 1860, Helmholtz related the magnitude of slip length to be on the order of the mean free path. During the past decades, a number of experimental (Vinogradova, 1999; Bonaccorso et al., 2002; Granick et al., 2003; Leger, 2003; Spikes and Granick, 2003; Vinogradova and Yakubov, 2006; Ho et al., 2011; Vinogradova and Belyaev, 2011) and simulation studies (Thompson and Troian, 1997; Barrat and Bocquet, 1999; Lichter et al., 2004; Priezjev and Troian, 2004; Priezjev, 2007; Huang et al., 2008; Liu and Li, 2010; Bao et al., 2017; Hu et al., 2017) have demonstrated that the slip length can be on the order of tens nanometers for liquids flowing over smooth nonwetting surfaces, and the μm scale slip lengths cannot be achieved without gas or air trapped at the surface.

* Corresponding author.

E-mail addresses: baoluyao@mail.nwpu.edu.cn (L. Bao), nikolai.priezjev@wright.edu (N.V. Priezjev), huhaiobao@nwpu.edu.cn (H. Hu).

When pockets of gas get trapped at the roughness of a hydrophobic surface, it usually acquires superhydrophobic properties. It should be noted that the micro/nano structures of SHS observed in nature are typically of irregular geometrical shape. To account for the influence of trapped gas on liquid slip in a more systematic way, man-made SHS with regularly arranged micro/nano structures are commonly manufactured and optimized for the enhanced slip properties (Ou and Rothstein, 2005; Choi and Kim, 2006; Byun et al., 2008; Crowdy, 2011). The indirect measurements of the effective slip length (ESL) based on pressure drop and flow rate, or direct measurements, using micro particle image velocimetry, demonstrated that the ESL on SHS can range from $1 \mu\text{m}$ ~ $200 \mu\text{m}$ depending on the GLI fraction and the shape of surface texture (Rothstein, 2010).

The concept of superhydrophobicity can also be extended to the nanoscale flows. For example, Cottin-Bizonne et al. (2003) investigated the slip behavior of a simple liquid on a solid surface with GLI width of about 6 atomic diameters using MD simulations. Their results indicated that the presence of GLI at nanostructured solid surface leads to ESL two times larger than the intrinsic slip length at the flat surface of the same material. Later, Tretyakov and Mueller (2012) systematically investigated the ESL and friction coefficient for different widths of rectangular ridges and grooves at the solid surface. Surprisingly, it was found that the shape of nanostructures had no influence on the slip length, although similar groove widths were considered for comparison with the work by Cottin-Bizonne et al. (2003). They attributed this result to the high interfacial friction resulting from the edges of the grooves (Tretyakov and Mueller, 2012). Furthermore, Yong and Zhang (2013) investigated the influence of nanobubble meniscus curvature on the ESL. They found that with increasing protrusion angles of a nanobubble, the ESL first increases and then decreases, and the ESL reaches its maximum at the protrusion angle of about 10° , which agrees with the results of Lattice Boltzmann simulations (Hyv luoma and Harting, 2008) and continuum fluid mechanics simulations (Steinberger et al., 2007).

Although the effective slip was repeatedly observed in experiments and simulations, the measurements of the local slip length (LSL) at GLI only recently attracted increased attention. In the analysis of the local slip, three distinct conjectures emerged; namely, (a) there is no shear stress at GLI, i.e., the LSL at GLI is infinite, which corresponds to the perfect slip at GLI (Lauga and Stone, 2003; Ou and Rothstein, 2005; Gogte et al., 2005; Choi and Kim, 2006), (b) the ESL is finite and constant at GLI (Belyaev and Vinogradova, 2010; Asmolov and Vinogradova, 2012; Zhou et al., 2013), (c) the LSL is finite and anisotropically distributed along the GLI (Sch necker and Hardt, 2013; Schnecker et al., 2014). All three assumptions regarding the LSL are widely used in interpretation of the experimental results (Ou and Rothstein, 2005; Gogte et al., 2005; Choi and Kim, 2006; Byun et al., 2008) and theoretical analysis (Lauga and Stone, 2003; Hyv luoma and Harting, 2008; Belyaev and Vinogradova, 2010; Schnecker et al., 2014). Recently, the anisotropic distribution of LSL at GLI was observed in experiments (Sch ffel et al., 2016) and MD simulations (Hu et al., 2018). By neglecting the influence of edges and assuming an explicit LSL distribution along the GLI, Schnecker et al. (2014) derived analytical expressions for the flow field as well as for the ESL in shear flow over a surface with periodic rectangular grooves. Although the analytical LSL deviated from the numerical values, Sch necker et al. showed that the assumption of the explicit LSL distribution is sufficiently accurate to reproduce flow fields that agree well with the results of numerical simulations. However, for nanoscale flows, the groove edge can significantly influence the LSL and flow field (Tretyakov and Mueller, 2012). Up to now, the local slip conditions and corresponding flow fields over nanoscale grooves were not thoroughly investigated. It should be emphasized that in mi-

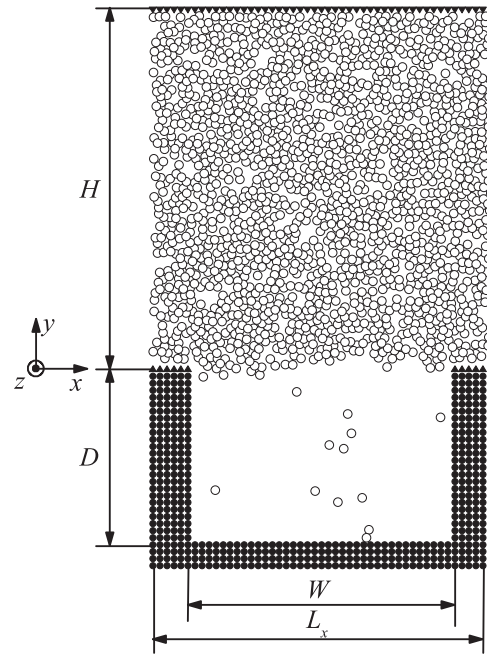


Fig. 1. The front view of the simulation model. H and L_x are the height and length of the channel, respectively. D and W are the depth and width of the groove, respectively.

cro/nano scale flows, the local flow characteristics are important for predicting flows in micro/nano fluidic devices. For example, Dubov et al. (2017) have shown that solid particles can be sorted in a transverse flow through grooved microchannels. In particular, the position-dependent velocity of the transverse flow causes neutrally buoyant particles to be displaced in the lateral direction, depending on their size and initial location, thus, leading to particle sorting (Dubov et al., 2017).

In this work, the LSL and flow field at SHS patterned with periodic rectangular grooves are systematically studied using MD simulations. A particular emphasis is placed on imposing a flat GLI by carefully adjusting the height of channel to make the bulk pressure equal to the coexistence pressure. We find that the slip velocity and shear rate at the GLI are well described by elliptical and exponential functions, respectively. With increasing groove width, two regimes of the local slip length distribution along the GLI are identified. At large GLI widths, both the groove edge and local hydrodynamics contribute to the interfacial friction, and the data for the normalized local slip length collapse onto a single curve for different groove widths. At small GLI widths, the normalized local slip length deviates from the master curve. Based on the simulation results, we propose an explicit function to describe the local slip boundary conditions for transverse and longitudinal flows. The proposed equation for LSL can be potentially used in the continuum analysis to model interfacial flows and avoid the necessity of considering gas flow inside surface protrusions.

2. Details of molecular dynamics simulations

In our setup, a Newtonian liquid is confined between two solid walls (see Fig. 1). The interaction between liquid atoms is modeled by the Lennard-Jones potential (LJ)

$$U_{LJ} = 4\varepsilon \left[\left(\frac{\sigma}{r} \right)^{12} - \left(\frac{\sigma}{r} \right)^6 \right], \quad (1)$$

where r is the distance between two atoms, and ε and σ are the characteristic energy and length of the LJ potential. The liquid

consists of 73728 atoms. The wall atoms also interact with liquid atoms through the LJ potential. The interaction potential is truncated at the cutoff radius $r_c = 2.5\sigma$. The characteristic length for the interaction between liquid and wall atoms is $\sigma_{WL} = 1.0\sigma$. The characteristic energy, ε_{WL} , is used to control the degree of wettability, e.g., $\varepsilon_{WL} = 1.0\varepsilon$ and $\varepsilon_{WL} = 0.01\varepsilon$ correspond to wetting and nonwetting substrates, respectively (Sendner et al., 2009).

The lower solid wall is constructed from the face-centred cubic (FCC) crystal using the lattice constant $\delta = 1.2\sigma$ with the (100) face in contact with the liquid. The density of the wall is $2.31\sigma^{-3}$. The upper wall consists of 2304 atoms arranged as a single layer, which bounds the liquid and induces shear flow. A rectangular groove is carved inside the lower wall to make the superhydrophobic surface. The geometrical dimensions of the simulation domain are depicted in Fig. 1. The dimension of the domain in the z -direction is $L_z = 28.8\sigma$ and in the x -direction is $L_x = 57.6\sigma$. The geometrical characteristics of the groove are denoted by the width, W , and depth, D . When W is equal to 7.2σ , 14.4σ , 21.6σ , 28.8σ , 36.0σ and 43.2σ , the number of atoms in the lower wall is 120,024, 105,336, 90,648, 75,960, 62,496, 46,584, respectively. At the lower wall, the sum of the groove width and the solid part along the x -direction is kept the same, i.e., the solid wall fraction decreases as the GLI fraction increases. The interaction energy between atoms of the upper wall and liquid atoms is $\varepsilon_{WL}^{\text{up}} = 1.0\varepsilon$. The atoms in the topmost layer of the lower wall also interact with liquid atoms with the energy, $\varepsilon_{WL}^{\text{down}} = 1.0\varepsilon$. The origin of the y -axis is set at the position of the topmost layer of the lower wall (see Fig. 1). The rest of atoms of the lower wall interact with liquid atoms with the energy of 0.01ε , which prevents the liquid from wetting the inner part of the groove, thus ensuring a stable GLI. The strength of the interaction between fluid and the upper wall, as well as the top most layer of lower wall is set to produce no-slip boundary condition, which corresponds to the commonly assumption of superhydrophobic surface in previous theoretical works (Philip, 1972; Lauga and Stone, 2003; Schönecker and Hardt, 2013; Schäffell et al., 2016). The smaller strength of $\varepsilon_{WL}^{\text{up}}$ or $\varepsilon_{WL}^{\text{down}}$ is able to cause intrinsic slip at the fluid-wall interface. According to the previous works, the intrinsic slip length of order 10σ (Priezjev and Troian, 2004; Priezjev, 2007; Bao et al., 2017; Hu et al., 2018) is comparable to the local slip length at the GLI. In our work, we focus on the situation where the no-slip boundary condition is valid on the fluid-wall interface, and leave the influence of intrinsic slip on the local slip at GLI in the future work. There is no interaction between wall atoms. The groove is filled by the liquid vapor to form the GLI. The position of the upper wall is used to control the bulk pressure of the liquid, thus adjusting the shape of the GLI to be flat (described in detail below). The upper wall is moving with a constant velocity, $U = 1.0\sigma/\tau$ in the $+x$ and $+z$ directions to generate the transverse and longitudinal shear flows. The maximum shear rate in the bulk of the liquid phase is $\dot{\gamma} \approx 0.017\tau^{-1}$. This value is small enough to ensure the flow remains laminar (Priezjev, 2007). The lower wall is kept stationary. Periodic boundary conditions are applied along both the x - and z -directions.

The simulations are carried out using the open-source MD code, LAMMPS (Plimpton, 1995), with timestep, $\Delta t = 0.002\tau$, where $\tau = \sqrt{m\sigma^2/\varepsilon}$, and m is the mass of liquid atoms. The Nosé-Hoover thermostat with the friction coefficient $\gamma = 0.2$ is used to keep the temperature of liquid at $T = 0.8\varepsilon/k_B$. For both type of flow, the thermostat is only applied in the directions perpendicular to the shear plane. The typical initial equilibration of the system was performed during the time interval of $2 \times 10^3\tau$. After equilibration, the flow reaches steady state after an additional time interval of $2 \times 10^3\tau$. Then, the entire simulation box is divided into bins parallel to the z -direction with $\Delta x = 1.0\sigma$ and $\Delta y = 1.0\sigma$ to compute

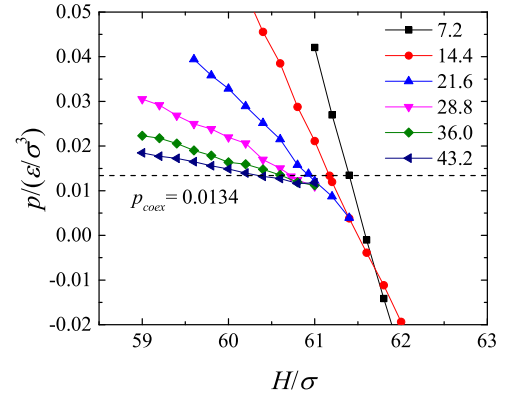


Fig. 2. Pressure of the liquid in the bulk region as a function of the channel height. The dashed line indicates the coexistence pressure. The widths of the groove, W , are listed in the legend.

the density and velocity fields. A typical time interval for averaging density and velocity fields is about $1.2 \times 10^4\tau$.

3. Results and discussions

3.1. Bulk pressure

In the previous theoretical and experimental studies (Lauga and Stone, 2003; Ou and Rothstein, 2005; Gogte et al., 2005; Choi and Kim, 2006; Byun et al., 2008; Belyaev and Vinogradova, 2010; Asmolov and Vinogradova, 2012; Schönecker and Hardt, 2013), the shape of GLI was assumed flat and parallel to the solid-liquid interface. In the present work, the GLI is made flat by controlling the bulk pressure of the liquid phase. Since the gas phase is the liquid vapor, the GLI is expected to be flat and parallel to the solid wall if the bulk pressure of the liquid is equal to the coexistence pressure. First, we calculated the coexistence pressure by considering a separate simulation setup where a slab of liquid is placed between two atomically smooth walls (see SI section). The liquid is in contact with the lower wall and there is a space between the liquid slab and the upper wall, which allows the vapor to fill the space spontaneously and generate a liquid-vapor coexistence state. The bulk pressure of the liquid slab is measured by calculating the local stress tensor, $p_{\alpha\beta}$, using the approach by Irving and Kirkwood (Kirkwood and Buff, 1949). More specifically, the simulation box of the liquid-vapor system is divided into slabs that are parallel to the solid wall. In the slab k , the local stress tensor, $p_{\alpha\beta}$, is defined as

$$p_{\alpha\beta} = \frac{1}{V_{sl}} \left\langle \sum_l m v_{l,\alpha} v_{l,\beta} \right\rangle + \frac{1}{V_{sl}} \left\langle \sum_{i<j} f_{\alpha,ij} \beta_{ij} \eta_k(\vec{r}_{ij}) \right\rangle, \quad (2)$$

where V_{sl} is the volume of the slab, $\alpha\beta$ is the combination of x , y , z , and $v_{l,\alpha} v_{l,\beta}$ is the product of the velocity components of the particle l located within the slab. The sum $\sum_{i<j}$ runs over particles i and j if a portion of the line connecting them is located inside the slab k . The parameter $\eta_k(\vec{r}_{ij})$ is the fraction of the connecting line that is located inside the slab k , and if both particles are in the slab k then $\eta_k(\vec{r}_{ij}) = 1$. At temperature, $T = 0.8\varepsilon/k_B$, the coexistence pressure is $p_{coex} = 0.0134\varepsilon/\sigma^3$ and the corresponding density of bulk liquid is $\rho_{coex} = 0.73\sigma^{-3}$.

Next, the magnitude of the coexistence pressure can be used as a criterion to control the shape of GLI by varying the position of the upper wall as shown in Fig. 1. Consequently, Fig. 2 shows the bulk pressure of liquid versus the height of the channel for different groove widths. The bulk pressure is calculated using Eq. (2). It can be clearly seen from Fig. 2 that the bulk pressure

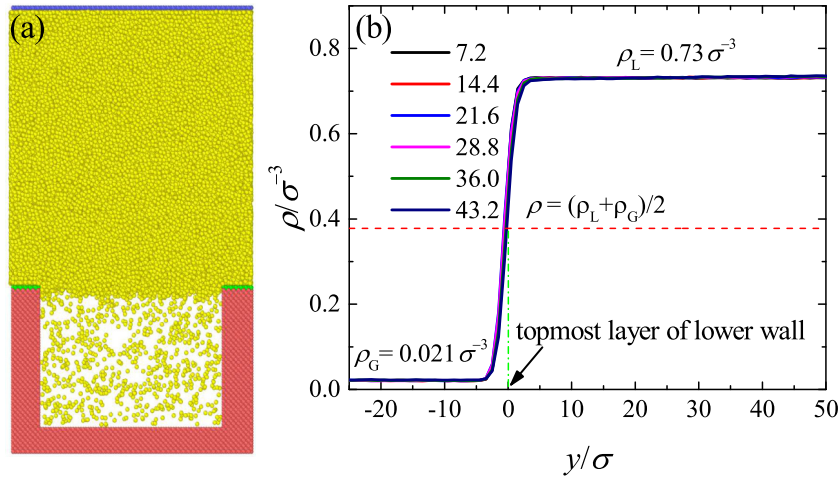


Fig. 3. (a) The snapshot of the system with the largest width of the groove ($W = 43.2\sigma$) during steady flow in the longitudinal direction. (b) The time-averaged density profiles perpendicular to the gas-liquid interface (GLI) at the center of GLI for the indicated groove widths.

Table 1

Values of the channel height, H , when the bulk pressure is equal to the coexistence pressure for different groove widths, W .

W/σ	H/σ
7.2	61.4
14.4	61.171
21.6	60.928
28.8	60.724
36.0	60.6
43.2	60.4

decreases with increasing channel height. As the bulk pressure becomes larger than the coexistence pressure, the GLI protrudes into the groove; otherwise, the GLI extends into the liquid phase (see SI section). If the bulk pressure is equal to the coexistence pressure, the GLI becomes flat. Hence, we determined the values of channel heights which make GLI flat for different groove widths. In what follows, these heights (see Table 1) will be used to carry out simulations in the presence of flow.

3.2. Flow fields for the transverse and longitudinal flow orientations

The representative snapshot of the sheared liquid confined between two walls is shown in Fig. 3(a) for the largest width of the groove ($W = 43.2\sigma$). It can be seen from Fig. 3(a) that the shape of the GLI is indeed flat. The position of the GLI can be quantitatively determined by examining the density profiles across the GLI. Here, we define the location of the GLI as the position where the density equals to half of the sum of liquid and gas densities, i.e., $\rho = \frac{1}{2}(\rho_L + \rho_G)$. It should be commented that previous studies (Tretyakov and Mueller, 2012) have shown that the degree of penetration of a liquid into the groove is controlled by the strength of the interaction energy between the liquid and solid atoms of the surface of the groove when the liquid pressure is equal to the coexistence pressure. In our work, the interaction energy between the liquid and solid atoms of the inner surface of the groove is very weak (0.01ϵ). Therefore, the liquid does not wet the inner part of the groove and the position of the GLI coincides with the topmost layer of the lower wall, as shown in Fig. 3(b). In the analysis below, the position of GLI is used to calculate the slip velocity and interfacial shear rate.

Fig. 4 presents the local velocity profiles perpendicular to the upper wall, i.e., along the y -direction for transverse and longitudinal flows. The width and depth of the groove are $W = 43.2\sigma$ and $D = 31.2\sigma$, respectively. Due to the symmetry with respect to the center of GLI, we only report the velocity profiles in the left part of the channel in Fig. 4(a) and (b). It is readily apparent that the presence of GLI significantly changes the local flow field. It can be seen in Fig. 4(a) (the transverse flow), the velocity profiles above GLI are curved, and the shear rate increases away from the location of GLI (along the y -direction). In other words, the shear stress decreases upon approaching the GLI, which is the main reason behind the drag reduction of SHS. It can be further observed in Fig. 4(a) that with x/W increasing from -0.09 to 0.49 , both the curvature of velocity profiles near the GLI and the slip velocity at the GLI increase. By contrast, the local velocity profile above the solid surface ($x/W = -0.09$) has an opposite curvature and zero slip velocity at the solid-liquid interface. It is interesting to note that the velocity profile immediately right of the groove edge ($x/W = 0.07$) almost coincides with the velocity profile above the solid surface. In other words, the shear stress at the groove edge and at the solid wall is nearly the same. In the bulk region far from the GLI, the perturbation of the velocity profiles due to GLI vanishes and they become linear. Inside the groove, the gas velocity is positive and negative in the vicinity of GLI and at bottom of the groove, indicating a vortex flow.

As is evident from Fig. 4(b), the local velocity fields for the longitudinal case are markedly different from the transverse case. Thus, the velocity profiles above the GLI are characterized by a pronounced slip velocity, which becomes larger near the center of the groove. Note however that the local slip condition at the solid-liquid interface is still no-slip. In addition, there is a finite slip velocity right off the groove edge in the longitudinal case but much smaller slip velocity in the transverse case. As expected, the gas velocity inside the groove is always parallel to the upper wall speed, as shown in Fig. 4(b).

Fig. 5 shows the slip velocity along the GLI for different groove widths for transverse and longitudinal flows. Note that the data for slip velocity are directly obtained from averaging within the narrow bin of 1.0σ at the GLI and solid-liquid interface. In all cases, the slip velocity increases upon approaching the center of GLI along the directions parallel to the xz -plane. It can also be seen that with increasing W , the slip velocity becomes larger in both transverse and longitudinal flows. In the previous theoretical studies (Schönecker and Hardt, 2013; Schneck et al., 2014), the

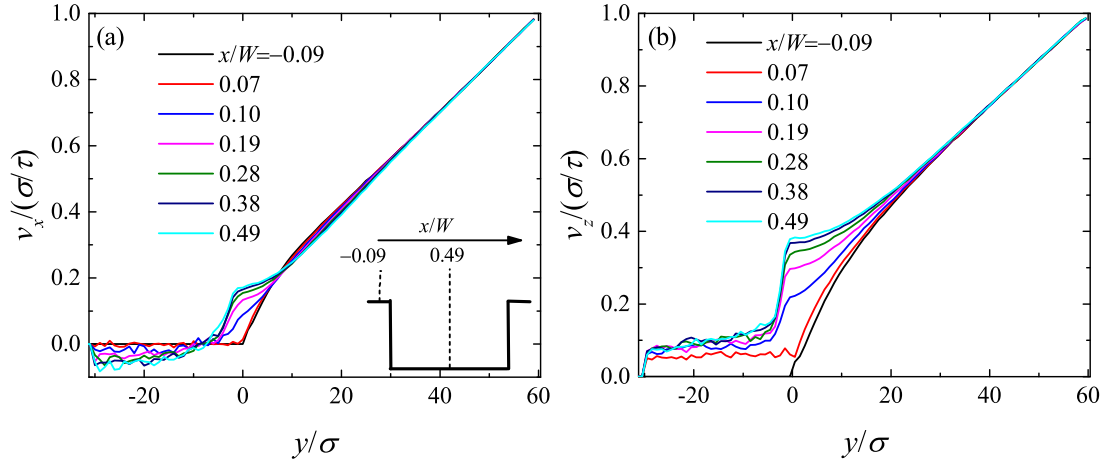


Fig. 4. The local velocity profiles along the y -direction for transverse (a) and longitudinal (b) flows. The values of x/W are the positions of averaging bins indicated by the dashed lines in the inset of panel (a). The origin of x/W starts from the left edge of the groove. The width and depth of the groove are $W = 43.2\sigma$ and $D = 31.2\sigma$, respectively. The left and right axes in the panels (a) and (b) indicate the locations of the bottom of the groove and the upper wall.

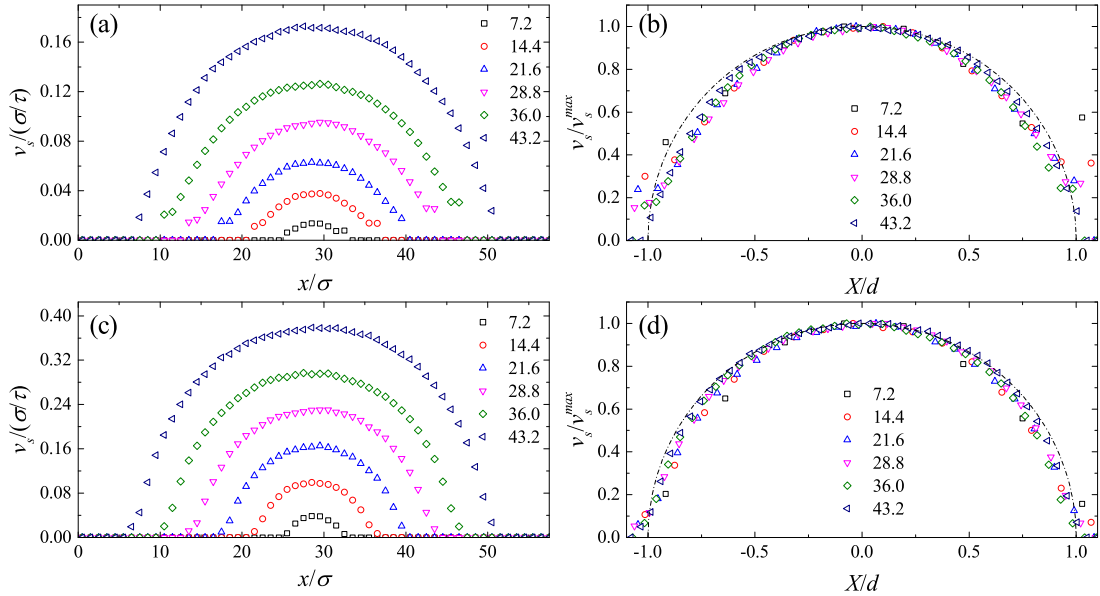


Fig. 5. The slip velocity along the gas-liquid interface (GLI) for the indicated groove widths for the transverse (a) and longitudinal (c) flows. The depth of the groove is $D = 31.2\sigma$. The data from panel (a) are replotted in the panel (b) with the slip velocity normalized using the maximum slip velocity and the location along the GLI divided by half the groove width. The same normalization procedure is implemented for the data in the panels (c) and (d). In panels (b) and (d), the normalized velocities are plotted with respect to the center of the groove. The dashed-dot lines are circles that are plotted for comparison with the simulation data.

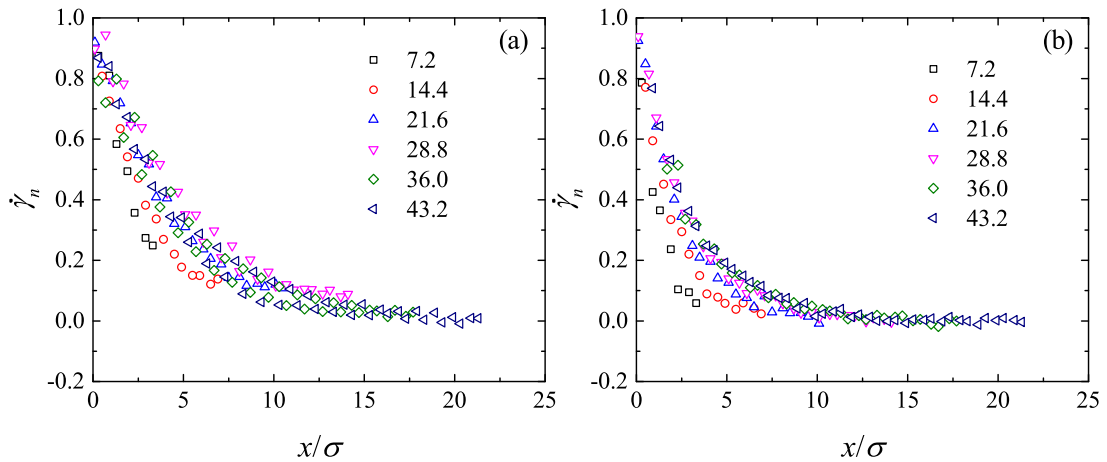


Fig. 6. The normalized local shear rate along the gas-liquid interface for the indicated groove widths for (a) transverse and (b) longitudinal flows. The depth of the groove is $D = 31.2\sigma$.

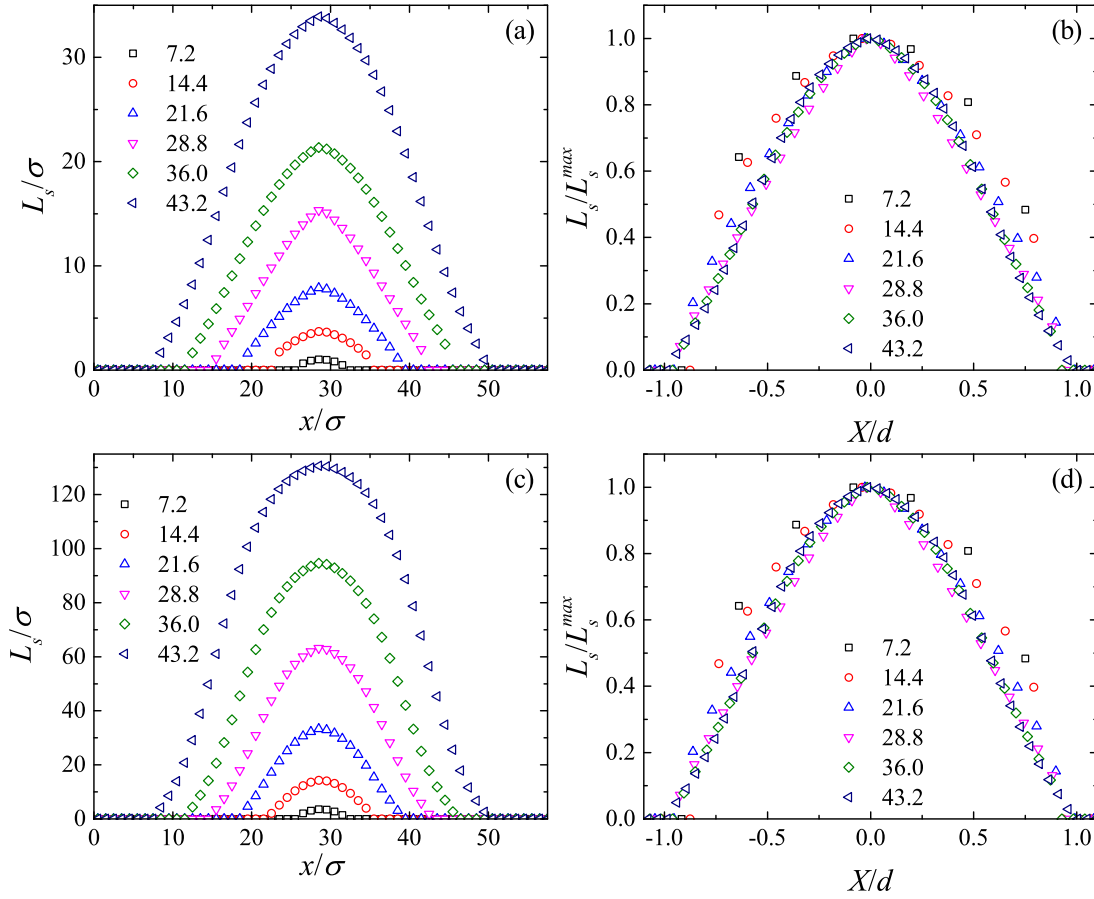


Fig. 7. The local slip length along the gas-liquid interface for transverse (a) and longitudinal (c) flows. The groove widths are indicated in the legends. The depth of the groove is $D = 31.2\sigma$. The data from panel (a) are replotted in the panel (b) with the local slip length normalized using the maximum LSL and the location along the GLI is divided by half the groove width. The same normalization procedure is used for the data in the panels (c) and (d). In panels (b) and (d), the normalized local slip lengths are plotted with respect to the center of the groove.

slip velocity along the GLI was described by an elliptical function. Fig. 5(b) and (d) shows the slip velocity normalized using the maximum value of the slip velocity for the corresponding width of the groove. Remarkably, all the data in both transverse and longitudinal cases collapse onto a single curve, which is well fitted using a circular function, $v_s/v_s^{max} = \sqrt{1 - X^2}$, where $X = x/d$ (d is half the width of the GLI). A similar elliptic profile for the slip velocity at the shear-free interface was also found by Philip (1972). Hence, we conclude that at the nanoscale, the slip velocity also obeys the elliptical distribution along the GLI.

3.3. The local slip length in transverse and longitudinal flows

In the previous section, it was shown that the slip velocity can be well described by an elliptical function. In the previous studies, the shear stress was assumed to be constant along the GLI leading to an explicit form for the local slip length distribution (Schönecker and Hardt, 2013; Schnecker et al., 2014). The assumption of a constant shear stress is reasonable when the width of groove is on the order of a micrometer, and the influence of the groove edges on the local slip length can be neglected. However, this is not the case in our situation, where the largest width of the groove is about 15 nm. To examine the slip boundary condition at the GLI, we next calculate the local slip length.

The LSL is computed using $L_s = v_s/\dot{\gamma}$, where $\dot{\gamma}$ is the local shear rate. It is well known that for flows over a homogeneous solid surface, the velocity profiles are simply linear and parabolic for Couette and Poiseuille flows, respectively. Correspondingly, the local

shear rate can be obtained by fitting the velocity profile in the bulk region and then extrapolating the fitting curve with respect to the solid-liquid interface (Lichter et al., 2004; Priezjev and Troian, 2004; Priezjev, 2007; Liu and Li, 2010; Bao et al., 2017). However, for a liquid flowing over SHS, the presence of GLI perturbs the flow field, which leads to spatially varying velocity profiles near the GLI (Schnecker et al., 2014). To simplify the fitting procedure, we follow the method used by Schäffel et al. (2016). They adopted a linear function to fit the velocity profiles near GLI to obtain the local shear rate.

In our study, the velocity profiles were fitted within 5σ above the GLI. The slip velocities calculated from the linearly fitted functions match well with the slip velocities averaged within narrow bins at GLI. The local shear rate is then extracted from the linear fit. We find that the local shear rate along the GLI can be well described by the exponential function, $\dot{\gamma} = \dot{\gamma}_0 + \dot{\gamma}_1 e^{-R_0 x}$ for different groove widths in both transverse and longitudinal flows. Here, $\dot{\gamma}_0$ is the shear rate at the center of GLI, and $\dot{\gamma}_1$ is the shear rate at the groove edge. R_0 represents the inverse scale for decay of the shear rate. A similar exponential decay of the shear rate was also presented in previous works (Schnecker et al., 2014). Fig. 6 shows the normalized local shear rate, $\dot{\gamma}_n = (\dot{\gamma} - \dot{\gamma}_0)/\dot{\gamma}_1$ along the GLI. Interestingly, the normalized local shear rate roughly follows a common curve for groove widths in the range from $W = 21.6\sigma$ to 43.2σ for both transverse and longitudinal flows. The local shear rate for groove widths $W = 7.2\sigma$ to 14.4σ deviates from the master curve. A similar behavior is also observed for LSL for different groove widths, see below.

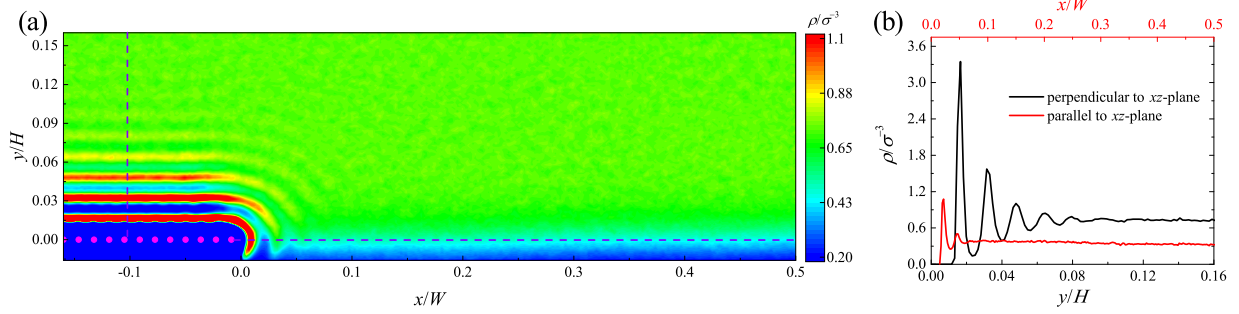


Fig. 8. (a) The density map near the left edge of the groove for the width, $W = 43.2\sigma$. The magenta circles represent the topmost layer of the lower wall. (b) The density profiles along the dashed lines shown in the panel (a).

In our analysis, we do not directly use the shear rate to compute the LSL, but instead extract the shear rate from the exponential function fitted to the shear rate along the GLI. Fig. 7 presents the LSL along the GLI for different groove widths. It can be seen that the LSL is finite for all groove widths considered in the present study. In particular, the LSL exhibits similar features for the transverse and longitudinal flows. The LSL becomes larger near the center of GLI. It is important to note that from the solid-liquid interface (no-slip region) to GLI (slip region), the LSL gradually increases from zero to a finite value. With increasing groove width, the LSL also increases. By examining the normalized data for LSL, similar to the shear rate, it becomes evident that the LSL exhibits two regimes depending on the groove width [see Fig. 7(b) and (d)]. In the first regime, i.e., $21.6\sigma \leq W \leq 43.2\sigma$, the data for LSL collapse onto a single curve. In the second regime, i.e., $W = 7.2\sigma$ to 14.4σ , the groove width, $W \leq 14.4\sigma$, the shear rate and LSL deviate from the master curves. In summary, we find that the slip velocity and shear rate along the GLI can be accurately described by the elliptical and exponential functions, respectively. Thus, the LSL follows $L_s = A\sqrt{1 - x^2/B^2}/(\dot{\gamma}_0 + \dot{\gamma}_1 e^{-R_0 x})$. It should be noted that the influence of edge on the LSL decays fast in an exponential way leading the edge effect can be neglected in the micro-size grooves. Therefore, our proposed function of LSL should be applicable for the case of nanosize grooves. Using the continuum approach, Nizkaya et al. (2014) found that the viscous dissipations near the edges of the grooves control the slopes of the LSL profiles and a power-law fits were proposed for the local and effective slip length. Our results indicate a different function form of LSL for nanosize grooves.

For liquids flowing over SHS with nanoscale grooves, the friction at the GLI originates from two factors. The first one is due to the viscous dissipation in the fluid (Schnecker et al., 2014). The other one is due to the edges of grooves (Tretyakov and Mueller, 2012). In the work by Müller and Tretyakov, the friction induced by the groove edge was attributed to the fluid layering near the groove edge. In our simulation setup, the interaction between atoms in the topmost layer of the lower wall and liquid atoms is very strong, $\varepsilon_{WL} = 1.0\varepsilon$. Therefore, the topmost layer of the lower wall induces fluid layering in the directions both perpendicular and parallel to the xz -plane (see Fig. 8). It can be seen from Fig. 8(b) that fluid layering in the direction perpendicular to the xz -plane extends up to about 6 liquid atomic diameters, which is consistent with the previous studies (Kaplan and Kauffmann, 2006; Kauffmann et al., 2011). In contrast, the fluid layering along the x -direction is only about 2 atomic diameters. Similar results were also observed by Fujiwara and Shibahara (2015). Our results of LSL and local shear rate indicate that the groove width required to separate two regimes is about 14.4σ . Therefore, the additional friction due to the groove edges does not originate only from the fluid layering near the edges. One possible reason leading to the

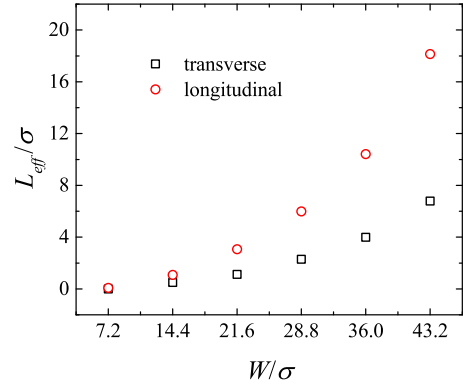


Fig. 9. The effective slip length as a function of the GLI width for transverse and longitudinal flows. The groove width is denoted as W .

two regimes of LSL is the influence of groove edges on the surface tension of GLI. It was shown by Fujiwara that the groove edge can affect the surface tension in the range of about 5–6 atomic diameters (Fujiwara and Shibahara, 2015), which is consistent with the estimate of the groove width ($\approx 14.4\sigma$) separating the two regimes of LSL in our study.

Finally, it is also instructive to calculate the ESL, which can be obtained by averaging the velocity profiles in the bulk region along the entire channel. The ESL is then calculated by linearly fitting the averaged velocity profile and extracting the effective slip velocity and shear rate at the location of GLI. The results are presented in Fig. 9. It can be clearly seen that the ESL increases with increasing groove width for both transverse and longitudinal flows. The ratio of the ESL in the transverse and longitudinal cases is about 2.6, while the ratio of LSL between the transverse and longitudinal cases is ≈ 3.8 . In the previous theoretical studies (Asmolov and Vinogradova, 2012; Schnecker et al., 2014), a different ratio between the LSL in the transverse and longitudinal cases are assumed to deduce the relationship between the ESL in the transverse and longitudinal cases. Our numerical results provide a reference to establish the relationship between the ESL in the transverse and longitudinal cases from the LSL.

4. Conclusions

In summary, we investigated the local slip behavior and flow fields of a simple liquid flowing over a superhydrophobic surface patterned with nanoscale rectangular grooves using molecular dynamics simulations. The groove is filled by the saturated vapor of the liquid, which results in the formation of a gas-liquid interface (GLI). The solid walls outside the GLI are set as hydrophilic to effectively impose the no-slip boundary condition at the solid-liquid

interface. The inner wall of the groove is nonwetting. By tuning the pressure in the bulk liquid to the coexistence pressure, a flat GLI is introduced parallel to the solid-liquid interface. This, in turn, allows us to compute precisely the local and effective slip lengths in both transverse and longitudinal flows. We found that the local slip velocity and shear rate are well described by elliptical and exponential functions, respectively. Based on these results, we proposed a functional form for the local slip length distribution along the GLI, i.e., $L_s = A\sqrt{1 - x^2/B^2}/(\dot{\gamma}_0 + \dot{\gamma}_1 e^{-R_0 x})$, which is valid for both transverse and longitudinal flows. Depending on the groove width, two regimes of the local slip length distribution along the GLI are identified. At the large GLI width regime, both the groove edges and local hydrodynamics contribute to the interfacial friction, and the normalized local slip lengths collapse onto a single curve at different groove widths. At the small GLI width regime, the groove edge dominates the friction at GLI, leading to deviation from the master curve obtained for wide grooves. Moreover, the numerical results indicate that the ratios of the effective and local slip lengths in the transverse and longitudinal cases are about 2.6 and 3.8, respectively. The proposed functional form for the local slip length is potentially useful for continuum modeling of liquid flows over grooved superhydrophobic surfaces without coupling to the gas flow inside the grooves.

Declaration of Competing Interest

The authors declare that they have no known competing financial interests or personal relationships that could have appeared to influence the work reported in this paper.

CRediT authorship contribution statement

Luyao Bao: Writing - original draft. **Nikolai V. Priezjev:** Writing - review & editing. **Haibao Hu:** Supervision.

Acknowledgments

This work was supported by the [National Natural Science Foundation of China](#) (grant numbers 51679203), the Basic frontier project (JCKY2018****18) and the [Fundamental Research Funds for the Central Universities](#) (no. 3102018gxc007). Computational work in support of this research was performed at National SuperComputer Center in Tianjin China.

Supplementary material

Supplementary material associated with this article can be found, in the online version, at doi:[10.1016/j.ijmultiphaseflow.2020.103258](https://doi.org/10.1016/j.ijmultiphaseflow.2020.103258).

References

Asmolov, E.S., Vinogradova, O.I., 2012. Effective slip boundary conditions for arbitrary one-dimensional surfaces. *J. Fluid Mech.* 706, 108–117.
 Bao, L., Priezjev, N.V., Hu, H., Luo, K., 2017. Effects of viscous heating and wall-fluid interaction energy on rate-dependent slip behavior of simple fluids. *Phys. Rev. E* 96 (3), 033110.
 Barrat, J.L., Bocquet, L., 1999. Large slip effect at a nonwetting fluid-solid interface. *Phys. Rev. Lett.* 82 (23), 4671–4674.
 Belyaev, A.V., Vinogradova, O.I., 2010. Effective slip in pressure-driven flow past super-hydrophobic stripes. *J. Fluid Mech.* 652, 489–499.
 Bonaccorso, E., Kappl, M., Butt, H.J., 2002. Hydrodynamic force measurements: boundary slip of water on hydrophilic surfaces and electrokinetic effects. *Phys. Rev. Lett.* 88 (7), 76103.
 Busse, A., Sandham, N.D., McHale, G., Newton, M.I., 2013. Change in drag, apparent slip and optimum air layer thickness for laminar flow over an idealised superhydrophobic surface. *J. Fluid Mech.* 727, 488–508.
 Byun, D., Kim, J., Ko, H.S., Park, H.C., 2008. Direct measurement of slip flows in superhydrophobic microchannels with transverse grooves. *Phys. Fluids* 20 (11), 113601.

Choi, C.H., Kim, C.J., 2006. Large slip of aqueous liquid flow over a nanoengineered superhydrophobic surface. *Phys. Rev. Lett.* 96 (6), 066001.
 Costantini, R., Mollicone, J.P., Battista, F., 2018. Drag reduction induced by superhydrophobic surfaces in turbulent pipe flow. *Phys. Fluids* 30 (2), 025102.
 Cottin-Bizonne, C., Barrat, J.-L., Bocquet, L., Charlaix, E., 2003. Low-friction flows of liquid at nanopatterned interfaces. *Nat. Mater.* 2 (4), 237–240.
 Crowdy, D., 2011. Frictional slip lengths for unidirectional superhydrophobic grooved surfaces. *Phys. Fluids* 23 (7), 072001.
 Dubov, A.L., Molotilin, T.Y., Vinogradova, O.I., 2017. Continuous electroosmotic sorting of particles in grooved microchannels. *Soft Matter* 13 (41), 7498–7504.
 Feuillebois, F., Bazant, M.Z., Vinogradova, O.I., 2009. Effective slip over superhydrophobic surfaces in thin channels. *Phys. Rev. Lett.* 102 (2), 026001.
 Fujiwara, K., Shibahara, M., 2015. Local pressure components and interfacial tensions of a liquid film in the vicinity of a solid surface with a nanometer-scale slit pore obtained by the perturbative method. *J. Chem. Phys.* 142 (9), 094702.
 Gogte, S., Vorobieff, P., Truesdell, R., Mammoli, A., van Swol, F., Shah, P., Brinker, C.J., 2005. Effective slip on textured superhydrophobic surfaces. *Phys. Fluids* 17 (5), 051701.
 Gose, J.W., Golovin, K., Boban, M., Mabry, J.M., Tuteja, A., Perlin, M., Ceccio, S.L., 2018. Characterization of superhydrophobic surfaces for drag reduction in turbulent flow. *J. Fluid Mech.* 845, 560–580.
 Granick, S., Zhu, Y.X., Lee, H., 2003. Slippery questions about complex fluids flowing past solids. *Nat. Mater.* 2 (4), 221–227.
 Ho, T.A., Papavassiliou, D.V., Lee, L.L., Striolo, A., 2011. Liquid water can slip on a hydrophilic surface. *Proc. Natl. Acad. Sci. USA* 108 (39), 16170–16175.
 Hu, H., Bao, L., Priezjev, N.V., Luo, K., 2017. Identifying two regimes of slip of simple fluids over smooth surfaces with weak and strong wall-fluid interaction energies. *J. Chem. Phys.* 146 (3), 034701.
 Hu, H., Wang, D., Ren, F., Bao, L., Priezjev, N.V., Wen, J., 2018. A comparative analysis of the effective and local slip lengths for liquid flows over a trapped nanobubble. *Int. J. Multiph. Flow* 104, 166–173.
 Huang, D.M., Sendner, C., Horinek, D., Netz, R.R., Bocquet, L., 2008. Water slippage versus contact angle: a quasiuniversal relationship. *Phys. Rev. Lett.* 101 (22), 226101.
 Hyväluoma, J., Harting, J., 2008. Slip flow over structured surfaces with entrapped microbubbles. *Phys. Rev. Lett.* 100 (24), 246001.
 Im, H.J., Lee, J.H., 2017. Comparison of superhydrophobic drag reduction between turbulent pipe and channel flows. *Phys. Fluids* 29 (9), 095101.
 Kaplan, W.D., Kauffmann, Y., 2006. Structural order in liquids induced by interfaces with crystals. *Annu. Rev. Mater. Res.* 36, 1–48.
 Kauffmann, Y., Oh, S.H., Koch, C.T., Hashibon, A., Scheu, C., Rühle, M., Kaplan, W.D., 2011. Quantitative analysis of layering and in-plane structural ordering at an alumina-aluminum solid-liquid interface. *Acta Mater.* 59 (11), 4378–4386.
 Kirkwood, J.G., Buff, F.P., 1949. The statistical mechanical theory of surface tension. *J. Chem. Phys.* 17 (3), 338–343.
 Lauga, E., Stone, H.A., 2003. Effective slip in pressure-driven stokes flow. *J. Fluid Mech.* 489, 55–77.
 Leger, L., 2003. Friction mechanisms and interfacial slip at fluid-solid interfaces. *J. Phys. Condens. Matter* 15 (1), S19–S29.
 Lichter, S., Roxin, A., Mandre, S., 2004. Mechanisms for liquid slip at solid surfaces. *Phys. Rev. Lett.* 93 (8), 086001.
 Liu, C., Li, Z.G., 2010. Surface effects on nanoscale poiseuille flows under large driving force. *J. Chem. Phys.* 132 (2), 024507.
 Martell, M.B., Rothstein, J.P., Perot, J.B., 2010. An analysis of superhydrophobic turbulent drag reduction mechanisms using direct numerical simulation. *Phys. Fluids* 22 (6), 065102.
 Nizkaya, T.V., Asmolov, E.S., Vinogradova, O.I., 2014. Gas cushion model and hydrodynamic boundary conditions for superhydrophobic textures. *Phys. Rev. E* 90, 043017.
 Nouri, N.M., Bakhsh, M.S., Sekhavat, S., 2013. Analysis of shear rate effects on drag reduction in turbulent channel flow with superhydrophobic wall. *J. Hydrodyn.* 25 (6), 944–953.
 Ou, J., Rothstein, J.P., 2005. Direct velocity measurements of the flow past drag-reducing ultrahydrophobic surfaces. *Phys. Fluids* 17 (10), 103606.
 Park, H., Sun, G.Y., Kim, C.J., 2014. Superhydrophobic turbulent drag reduction as a function of surface grating parameters. *J. Fluid Mech.* 747, 722–734.
 Philip, J.R., 1972. Flows satisfying mixed no-slip and no-shear conditions. *Z. Angew. Math. Phys. ZAMP* 23 (3), 353–372.
 Plimpton, S., 1995. Fast parallel algorithms for short-range molecular-dynamics. *J. Comput. Phys.* 117 (1), 1–19.
 Priezjev, N.V., 2007. Effect of surface roughness on rate-dependent slip in simple fluids. *J. Chem. Phys.* 127 (14), 144708.
 Priezjev, N.V., Troian, S.M., 2004. Molecular origin and dynamic behavior of slip in sheared polymer films. *Phys. Rev. Lett.* 92 (1), 018302.
 Rastegari, A., Akhavan, R., 2019. On drag reduction scaling and sustainability bounds of superhydrophobic surfaces in high reynolds number turbulent flows. *J. Fluid Mech.* 864, 327–347.
 Rothstein, J.P., 2010. Slip on superhydrophobic surfaces. *Annu. Rev. Fluid Mech.* 42 (1), 89–109.
 Schäffle, D., Koyunov, K., Vollmer, D., Butt, H.-J., Schoenecker, C., 2016. Local flow field and slip length of superhydrophobic surfaces. *Phys. Rev. Lett.* 116 (13), 134501.
 Schnecker, C., Baier, T., Hardt, S., 2014. Influence of the enclosed fluid on the flow over a microstructured surface in the Cassie state. *J. Fluid Mech.* 740, 168–195.
 Schönecker, C., Hardt, S., 2013. Longitudinal and transversal flow over a cavity containing a second immiscible fluid. *J. Fluid Mech.* 717 (2), 376–394.

- Sendner, C., Horinek, D., Bocquet, L., Netz, R.R., 2009. Interfacial water at hydrophobic and hydrophilic surfaces: Slip, viscosity, and diffusion. *Langmuir* 25 (18), 10768–10781.
- Song, D., Daniello, R., Rothstein, J., 2014. Drag reduction using superhydrophobic sanded teflon surfaces. *Exp. Fluids* 55, 1783.
- Spikes, H., Granick, S., 2003. Equation for slip of simple liquids at smooth solid surfaces. *Langmuir* 19 (12), 5065–5071.
- Srinivasan, S., Kleingartner, J.A., Gilbert, J.B., Cohen, R.E., Milne, A.J.B., McKinley, G.H., 2015. Sustainable drag reduction in turbulent Taylor-Couette flows by depositing sprayable superhydrophobic surfaces. *Phys. Rev. Lett.* 114 (1), 14501.
- Steinberger, A., Cottin-Bizonne, C., Kleimann, P., Charlaix, E., 2007. High friction on a bubble mattress. *Nat. Mater.* 6 (9), 665–668.
- Thompson, P.A., Troian, S.M., 1997. A general boundary condition for liquid flow at solid surfaces. *Nature* 389 (6649), 360–362.
- Tretyakov, N., Mueller, M., 2012. Correlation between surface topography and slippage. *Soft Matter* 9 (13), 3613–3623.
- Vinogradova, O.I., 1999. Slippage of water over hydrophobic surfaces. *Int. J. Miner. Process.* 56 (1–4), 31–60.
- Vinogradova, O.I., Belyaev, A.V., 2011. Wetting, roughness and flow boundary conditions. *J. Phys. Condens. Matter* 23 (18), 184104.
- Vinogradova, O.I., Yakubov, G.E., 2006. Surface roughness and hydrodynamic boundary conditions. *Phys. Rev. E* 73 (4), 045302.
- Yong, X., Zhang, L.T., 2013. Toward generating low-friction nanoengineered surfaces with liquid-vapor interfaces. *Langmuir* 29 (41), 12623–12627.
- Zhang, J.X., Tian, H.P., Yao, Z.H., Hao, P.F., Jiang, N., 2015. Mechanisms of drag reduction of superhydrophobic surfaces in a turbulent boundary layer flow. *Exp. Fluids* 56 (9), 179.
- Zhou, J., Asmolov, E.S., Schmid, F., Vinogradova, O.I., 2013. Effective slippage on superhydrophobic trapezoidal grooves. *J. Chem. Phys.* 139 (17), 174708.